Efficacy, long-term toxicity, and mechanistic studies of gold nanorods photothermal therapy of cancer in xenograft mice

Moustafa R. K. Ali[a,1], Mohammad Aminur Rahman[b,1], Yue Wu[a], Tiegang Han[c], Xianghong Peng[b], Megan A. Mackey[a], Dongsheng Wang[b], Hyung Ju Shin[d], Zhuo G. Chen[b], Haopeng Xiao[a], Ronghu Wu[a], Yan Tang[c], Dong M. Shin[b,2], and Mostafa A. El-Sayed[a,e,2]

[a]School of Chemistry and Biochemistry, Georgia Institute of Technology, Atlanta, GA 30332; [b]Department of Hematology and Medical Oncology, Winship Cancer Institute, Emory University School of Medicine, Atlanta, GA 30322; [c]School of Biology, Georgia Institute of Technology, Atlanta, GA 30332; [d]Quest Diagnostics, Atlanta, GA 30308; and [e]School of Chemistry, King Abdul Aziz University, Jeddah 23218, Kingdom of Saudi Arabia

Gold nanorods (AuNRs)-assisted plasmonic photothermal therapy (AuNRs-PPTT) is a promising strategy for combating cancer in which AuNRs absorb near-infrared light and convert it into heat, causing cell death mainly by apoptosis and/or necrosis. Developing a valid PPTT that induces cancer cell apoptosis and avoids necrosis in vivo and exploring its molecular mechanism of action is of great importance. Furthermore, assessment of the long-term fate of the AuNRs after treatment is critical for clinical use. We first optimized the size, surface modification [rifampicin (RF) conjugation], and concentration (2.5 nM) of AuNRs and the PPTT laser power (2 W/cm^2) to achieve maximal induction of apoptosis. Second, we studied the potential mechanism of action of AuNRs-PPTT using quantitative proteomic analysis in mouse tumor tissues. Several death pathways were identified, mainly involving apoptosis and cell death by releasing neutrophil extracellular traps (NETs) (NETosis), which were more obvious upon PPTT using RF-conjugated AuNRs (AuNRs@RF) than with polyethylene glycol thiol-conjugated AuNRs. Cytochrome c and p53-related apoptosis mechanisms were identified as contributing to the enhanced effect of PPTT with AuNRs@RF. Furthermore, Pin1 and IL18-related signaling contributed to the observed perturbation of the NETosis pathway by PPTT with AuNRs@RF. Third, we report a 15-month toxicity study that showed no long-term toxicity of AuNRs in vivo. Together, these data demonstrate that our AuNRs-PPTT platform is effective and safe for cancer therapy in mouse models. These findings provide a strong framework for the translation of PPTT to the clinic.

gold nanorods | plasmonic photothermal therapy | apoptosis | xenograft mice | long-term toxicity

P lasmonic photothermal therapy (PPTT) has recently drawn considerable attention for cancer treatment, because plasmonic nanoparticles can effectively convert absorbed near-infrared (NIR) light into heat that ultimately kills cancer cells (1–4). Gold nanorods (AuNRs) show unique physicochemical properties compared with other gold nanoparticles (5, 6), in that they absorb and scatter NIR radiation (650–900 nm) strongly and have suitable aspect ratios (length divided by width). AuNRs have been found to be one of the most effective photothermal contrast agents (7, 8). PPTT can induce cell death mainly via two pathways: necrosis and apoptosis (9). During necrosis, the heat induced by PPTT (if above 50 °C) could disrupt the plasma membrane, causing the cellular components to leak out and cause inflammation, metastasis (10), and harm to surrounding normal tissues. Apoptosis is a programmed cell death pathway that triggers cancer cell death (11, 12), attenuates inflammatory activities, and is regarded as a "cleaner" process of cell elimination. Skewing the response toward apoptotic cell death rather than necrotic death will minimize inflammatory responses that may promote the damage or destruction of healthy tissues. Therefore, modulating PPTT to trigger apoptosis would be more favorable in clinical settings (7, 13) It has been reported that different intracellular locations or shapes of nanoparticles potentially

regulate the switch between necrosis and apoptosis (14). In this study, we aimed to optimize the conditions of AuNRs-PPTT to trigger apoptosis rather than necrosis and examined the molecular impact of AuNRs-PPTT in vivo using Western-blot analysis and MS-based proteomics.

To optimize the efficacy of apoptosis induction, we considered several aspects of the fabrication of AuNRs (i.e., the size, dose, and surface modifications of AuNRs) to enhance the internalization of AuNRs and the generation of heat. Effective internalization of AuNRs in tumor tissue is a significant challenge (15–18). To increase the uptake of AuNRs, surface modification with ligands that assist endocytosis or block exocytosis has been used, aiming at greater nanoparticle retention inside cancer cells (19). We have previously developed rifampicin (RF)-conjugated AuNRs for the purpose of enhancing the internalization of AuNRs in tumor cells. RF was shown to enhance the entry of AuNRs into cells and decrease exocytosis from the cells (20). However, detailed mechanisms of the behavior of RF-coated AuNRs in vivo have yet to be explored. Heat generation and dose of the AuNRs must also be considered (21).

To better understand the cellular responses to PPTT, more systematic studies in vivo are required. Most previous reports concerning the mechanism of PPTT were only conducted in vitro (14) and focus on a single protein or pathway. Several mechanisms

have been proposed in vitro. Ali et al. (13) proposed heat shock protein 70 as a major player. Pérez-Hernández et al. (14) reported that apoptosis during PTT using gold nanoprisms is mediated by the proteins Bak and Bax, through the activation of the protein Bid. To better understand the mechanisms involved, systematic analysis such as MS-based proteomics is necessary.

The safety profile of AuNRs remains largely undefined (22). Gold is a chemically inert material. Therefore, it is generally considered biocompatible and has been used in some routine clinical practices for many years (e.g., in treating rheumatoid arthritis). Several studies have reported no significant short-term toxicity of AuNPs (1 day to 3 months) (23–25). You et al. (26) have reported a lack of both acute and chronic toxicity over 3 months following multiple injections of PEGylated hollow gold nanospheres in mice. However, other studies have contradictorily reported that the presence of nanoparticles causes cytotoxicity such as actin stress (27), induces apoptosis, or causes inflammation in mouse livers (28). Some studies have explored how gold nanoparticle exposure (aside from any heat-induced effects) affects cells at the molecular level, affects pathways such as mitochondrial oxidative phosphorylation, and causes oxidative stress (29). The dose-dependent effects of gold nanoparticles on biological systems have been widely recognized (30). A high dose of NPs or the desorbed surfactants from their surface could result in "toxic" behavior (31, 32). Of concern for AuNRs is the incomplete purification of surfactant cetyltrimethylammonium bromide (CTAB), which may cause cytotoxicity (33). Therefore, the optimal dose and purification of AuNRs is of great importance in minimizing toxic effects. The preservation of spherical AuNPs without complete clearance over 6 months has been reported (34). You et al. (26) also reported slow clearance of gold nanoparticles from the body during the 3-month period. Such body deposition of metallic NPs over a long time period raises significant concerns regarding their long-term safety. Therefore, a comprehensive investigation of the organ uptake, biodistribution, longer-term fate, and toxicity of AuNRs is essential to fundamentally understand their in vivo biological interactions and to use this knowledge to minimize their toxicity (24).

Here, we report the long-term in vivo fate of AuNRs 15 months after the initial administration, their biodistribution and associated toxicity in a BALB/c mouse model, and their efficacy in a head and neck squamous cell carcinoma (HNSCC) xenograft model. Our findings add to the current knowledge of AuNRs-PPTT in vivo in regulating apoptosis signaling and providing an effective and safe potential new treatment. This study provides a strong framework for the translation of this approach to the clinic.

Results

Efficacy of AuNR@RF/PPTT in Cellular Growth Inhibition in Vitro (HNSCC Cells) and in Tumor Growth Reduction in an MDA686TU Xenograft Model.
AuNRs were synthesized using a seedless growth technique (35). AuNRs were conjugated with BSA as a protein carrier and linker to RF, as shown in schematic Fig. 1A. Detailed descriptions of AuNRs synthesis, conjugation, cellular uptake, and cytotoxicity measurements are in *Supporting Information*. Briefly, transmission electron microscope (TEM) images (Fig. S1A) show the average size of AuNRs [for small AuNRs: 25 ($\pm$ 3) nm $\times$ 5.5 ($\pm$ 0.8) nm (length $\times$ width), and for big AuNRs: 72 ($\pm$ 7) nm $\times$ 16 ($\pm$ 4) nm] and the UV-visible (UV-Vis) spectrum shows an absorbance centered near 800 nm, corresponding to the longitudinal surface plasmon resonance band of AuNRs (Fig. S1B). Successful conjugation of BSA/RF molecules to the surface of AuNRs (AuNRs@BSA@RF) was proven by red shift of the plasmon peak of AuNRs in the UV-Vis spectrum (Fig. S1B), fluorimetry (Fig. S1C), and zeta potential (Fig. S1D). Successful uptake of AuNRs@RF was observed by 3D scanning differential interference contrast (DIC) microscopy (Fig. 1B and Fig. S2), dark-field images (Fig. S1E), and UV-Vis absorbance (Fig. S1F). After applying PPTT to AuNRs@RF, the release of RF molecules from the surface of AuNRs, as shown in

schematic Fig. 1A, was demonstrated by UV-Vis spectra (Fig. S1B). After PPTT, the RF peaks of the particles (330 nm and 470 nm) disappeared, accompanied by increased concentration of RF in the supernatant, indicating the release of surface RF. The number of RF molecules per AuNRs was calculated according to a previous study (36). From the calculation, we found 657 RF molecules present on each AuNRs@BSA, most of which was released after PPTT as shown in Fig. S1B by the loss of RF peaks on AuNRs. Furthermore, DIC images (Fig. 1B) show increases in the sizes of nanoparticle aggregates after PPTT, further supporting the release of surface ligands after PPTT (shown in Fig. 1A) which causes the particles to more easily aggregate. Similarly, AuNRs@PEG were also prepared, and their detailed characterization is described in *Supporting Information* (Fig. S3).

The effectiveness of PPTT in the regulation of cell viability was examined in five HNSCC cell lines, MDA686TU, Fadu, UD-SCC2, UM-SCC-47, and SqCC/Y1. We applied different concentrations of AuNRs@PEG with 2 W/cm^2 laser to optimize the AuNRs concentration. We found inhibition of cell viability (~30–50%) following treatment with at least 2.5 nM AuNRs@PEG compared with nontreated cell lines after 72 h (Fig. S4A). Furthermore, we compared the effectiveness of AuNRs@RF and AuNRs@PEG in MDA686TU cells. Interestingly, we observed that AuNRs@RF/PPTT reduced cell viability more efficiently than AuNRs@PEG/PPTT (Fig. S4B). We also observed that treatment with both AuNRs@RF and AuNRs@PEG mainly induced apoptosis without obvious necrotic death (Fig. S4C). These observations prompted us to further investigate the mechanistic details of AuNRs@RF action. In MDA686TU cells treated with AuNRs@PEG or AuNRs@RF followed by laser treatment, RF-conjugated AuNRs induced approximately twice as much apoptosis compared with AuNRs@PEG/PPTT alone (Fig. 1C and Fig. S4B). Western-blot analysis revealed that AuNRs-PPTT induced apoptotic signaling molecules such as cleaved caspase 3 (effector caspase), followed by cleavage of substrate poly ADP ribose polymerase (PARP) (Fig. 1D). In addition, we observed that AuNRs@RF/PPTT reduced cell viability and proliferation, evidenced by reduction of Akt and Erk activation and up-regulation of the cell cycle inhibitor protein p21 (Fig. 1D).

To optimize AuNRs concentration and laser power and assess anticancer therapeutic potential in vivo, we established an MDA686TU xenograft model. We applied three concentrations of AuNRs (conjugated with PEG or RF), 2.5, 5, and 10 nM, along with three different powers of laser, 0.5, 1, and 2 W/cm^2. In addition, we compared two different sizes of AuNRs@PEG (the characterization of big AuNRs is shown in Fig. S5) due to their different heat conversion capacities. Nanoparticles (100 μL) were injected intratumorally and laser treatment was performed once on day 1. We included three control groups: PBS, AuNRs (without laser), and laser alone. Tumor progression data over 25 days in mice from each treatment group are presented in Fig. 1E and Figs. S6 and S7, with the corresponding mice shown in Fig. 1F. We observed promising tumor growth inhibition with smaller-sized AuNRs@PEG. Over 25 days, tumor growth was reduced significantly in mice treated with AuNRs@PEG at all three concentrations only when the laser power was 2 W/cm^2 (Fig. 1E). We observed that treatment with 10 nM and 5 nM AuNRs@PEG with 2 W/cm^2 laser reduced tumor growth by manyfold compared with the control groups (PBS, laser only, and AuNRs only) (Fig. 1E) [control groups (PBS, laser, or AuNRs) vs. treated groups (2.5, 5, or 10 nM AuNRs@PEG-PPTT), $P < 0.01$]. However, we observed skin wounding effects in mice at these concentrations (Fig. 1F). Treatment with 2.5 nM AuNRs@PEG-PPTT had a moderate wounding effect; however, tumor growth increased after 20 days (Fig. 1E). In comparison with 2.5 nM small AuNRs@PEG (25-nm length), treatment with 2.5 nM large (72-nm length) AuNRs@PEG-PPTT had no obvious effect on tumor inhibition (Fig. 1E). Because AuNRs@RF-PPTT showed the most efficient apoptosis in vitro
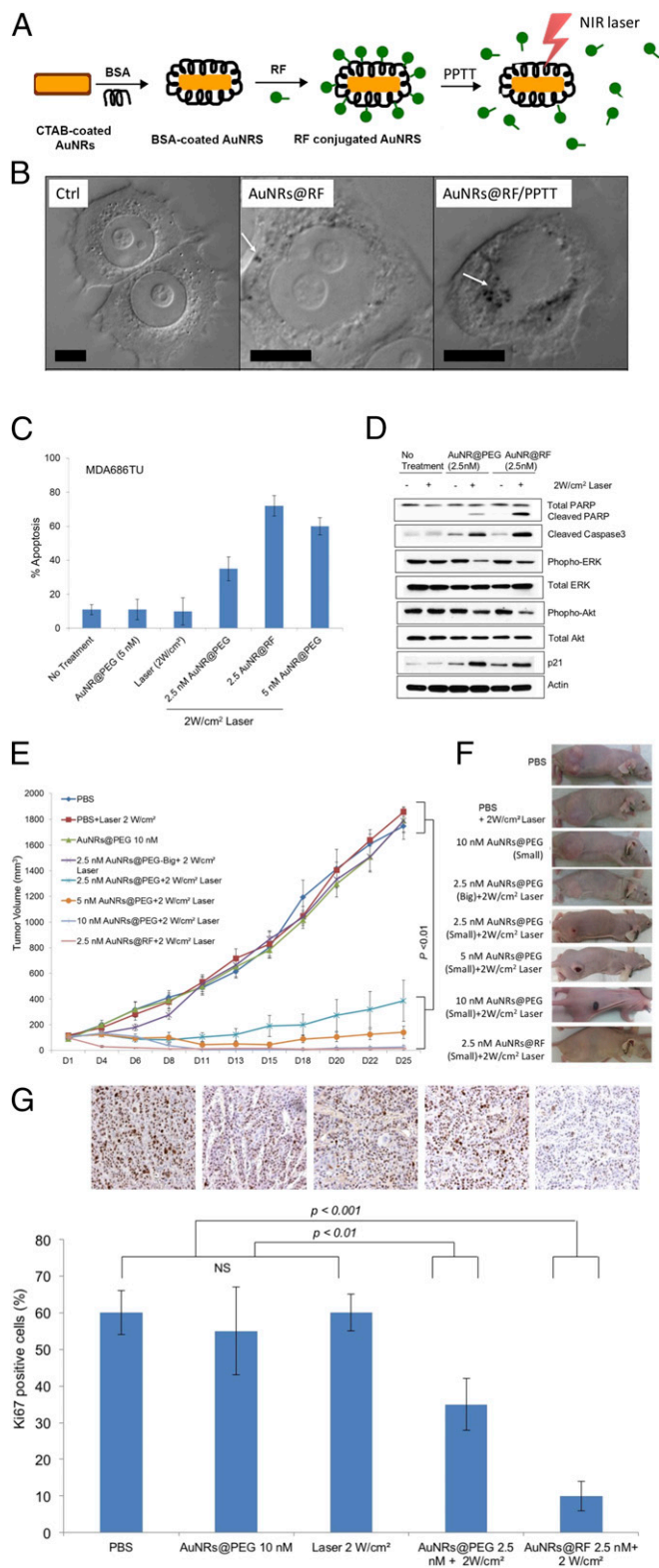
Fig. 1. Efficacy of AuNRs@RF in vivo and in vitro. (*A*) Schematic showing the characterization and conjugation of AuNRs@Rifampicin and the release of surface ligands after PPTT. (*B*) DIC images of optical sectioning of control sample (without nanoparticles), cells incubated with AuNRs@RF, and cells after PPTT. White arrows indicate AuNRs aggregates. (Scale bars, 10 μm.) (*C*) Comparative apoptosis analysis in MDA686TU HNSCC cells treated with AuNRs or AuNRs@RF and PPTT after 72h (error bars are mean ± SD, *n* = 3). (*D*) Western blotting for the indicated proteins in MDA686TU HNSCC cell line after treatment with AuNRs@PEG-PPTT and AuNRs@RF-PPTT. A representa-

(Fig. 1*C*), we were interested to see the effect in vivo in comparison with AuNRs@PEG-PPTT. We found that 2.5 nM AuNRs@RF-PPTT efficiently reduced tumor growth to the same extent as 10 nM AuNRs@PEG-PPTT without any skin wounding (Fig. 1 *E* and *F*) [control groups (PBS, laser, or AuNRs) vs. treated group (2.5 nM AuNRs@RF-PPTT), *P* < 0.01]. All mice were killed on day 25 and tumors were collected. Tumor weight was significantly reduced in mice treated with all concentrations of small AuNRs with 2 W/cm² laser (Fig. S6) [control (PBS, laser, or AuNRs) vs. treated groups, *P* < 0.01], whereas large AuNRs (Fig. S6) or lower laser power was unable to reduce tumor growth (Fig. S7). The mice were monitored during and after tumor cell and nanoparticle injections. Movement, diet, and vital signs (ruffled fur, weight loss, and normal activity) were observed throughout the experiments. We did not observe any abnormalities other than the skin wounding effect at higher concentrations of AuNRs. Immunohistochemistry (IHC) of mouse tumor tissues for the cell proliferation marker Ki67 (Fig. 1*G*) suggested that AuNRs@RF (25-nm length) with 2 W/cm² laser significantly reduced cell viability, accompanied by the suppression of tumor growth progression without any skin wounding effect.

AuNRs@RF-PPTT Induces Stronger Perturbation of Apoptosis and Cell Death by Releasing Neutrophil Extracellular Traps (NETosis) Pathway. We conducted quantitative proteomics experiments using tandem mass tags (TMT) to study alterations in protein expression levels in tumor tissues, identify the mechanisms responsible for the induction of apoptosis by AuNRs@PEG-PPTT and AuNRs@RF-PPTT, and explore why AuNRs@RF-PPTT was much more effective. Two biological replicates were conducted for AuNRs@PEG-PPTT-treated, AuNRs@RF-PPTT-treated, and control groups. Differentially expressed proteins identified in each experiment (AuNRs@PEG-PPTT and AuNRs@RF-PPTT) were compared (Fig. 2*A*). In total, we measured 5,222 proteins. For proteomics analysis, we set ±0.5 as a threshold for fold change (log 2) detection (Fig. 2*B*). Following AuNRs@PEG-PPTT treatment, 532 proteins were decreased and 600 proteins were increased. AuNRs@RF-PPTT treatment led to down-regulation of 558 and up-regulation of 644 proteins (Fig. 2*C*). Overlap in altered proteins (increased or decreased) is shown in Fig. 2*D*.

Pathway analysis identified apoptosis-related pathways that were significantly regulated by AuNRs@RF-PPTT and AuNRs-PPTT compared with the control group (Fig. 2*F*), including Granzyme B signaling, phosphorylation of protein BAD (BCL2 associated agonist of cell death), caspase cascade, and others. These pathways and associated increased proteins (Fig. 2*E* and Dataset S1) may provide a mechanistic explanation for the apoptosis-promoting effect of PPTT with AuNRs. Apoptosis-related proteins are listed in Fig. 2*E* and a schematic illustration is shown in Fig. 2*G*. A greater increase in cytochrome *c* and Apaf-1 protein expression was identified following AuNRs@RF-PPTT vs. AuNRs@RF treatment. Cytochrome *c* and Apaf-1 form a complex leading to the activation of caspase-9,

tive blot of three independent experiments is presented. (*E*) MDA686TU HNSCC tumor xenograft growth (tumor volume = 0.5×l×w2) progression in groups: PBS, 2 W/cm² laser, 10 nM small AuNRs@PEG as control groups; 5 nM, 10 nM small AuNRs@PEG with 2W/cm² laser; 2.5 nM small and large AuNR@PEG with 2 W/cm² laser; 2.5 nM AuNRs@RF with 2 W/cm² laser. First and only dose was given on day 1 (tumor volume ~70 mm³) and tumor growth was monitored until day 25 (endpoint of tumor volume 1,800 mm³) (error bars are mean ± SEM, *n* = 5). Statistical analysis (*t* test) between control groups (PBS, laser, and AuNRs@PEG) vs. treated groups (2.5, 5, and 10 nM AuNRs@PEG-PPTT, 2.5 nM AuNRs@RF-PPTT) was *P* < 0.01. (*F*) Representative mouse from each of the indicated groups presented. (*G*) Ki-67 expression detected in xenograft tissue by IHC analysis. Representative images shown from indicated groups (brown stain for Ki-67 and nuclei were counterstained by hematoxylin, blue; magnification ×200). For comparison with other studies, 5 nM = 1 OD for small AuNRs (35).

which activates caspase-3, inducing caspase-3–mediated apoptosis (37, 38). In addition, we observed the activation of upstream signaling of p38alpha, which leads to ROS generation (39, 40) that can result in mitochondrial dysfunction-triggered apoptosis. We also observed increased levels of FANCD2 (Fanconi anemia complementation group D2), tumor suppressor protein p53, and PTEN (phosphatase and tensin homolog). FANCD2 is required for the maintenance of chromosomal stability, which is involved in the repair of DNA double-strand breaks (41, 42). DNA damage can

affect FANCD2 via FANCL (Fanconi anemia complementation group L) (43, 44), whereas FANCD2 can further interact with tumor suppressor protein BRCA1 (45, 46). BRCA1 then activates CHK1 (checkpoint kinase 1) (47), which activates p53 (48). Activated p53 then promotes apoptosis (49). PTEN can also induce apoptosis via PI3K/AKT-dependent and -independent pathways (50) or other pathways (51, 52). We observed stronger apoptosis promotion (i.e., greater up-regulation of apoptosis-related proteins) with AuNRs@RF-PPTT compared with AuNRs@PEG-PPTT
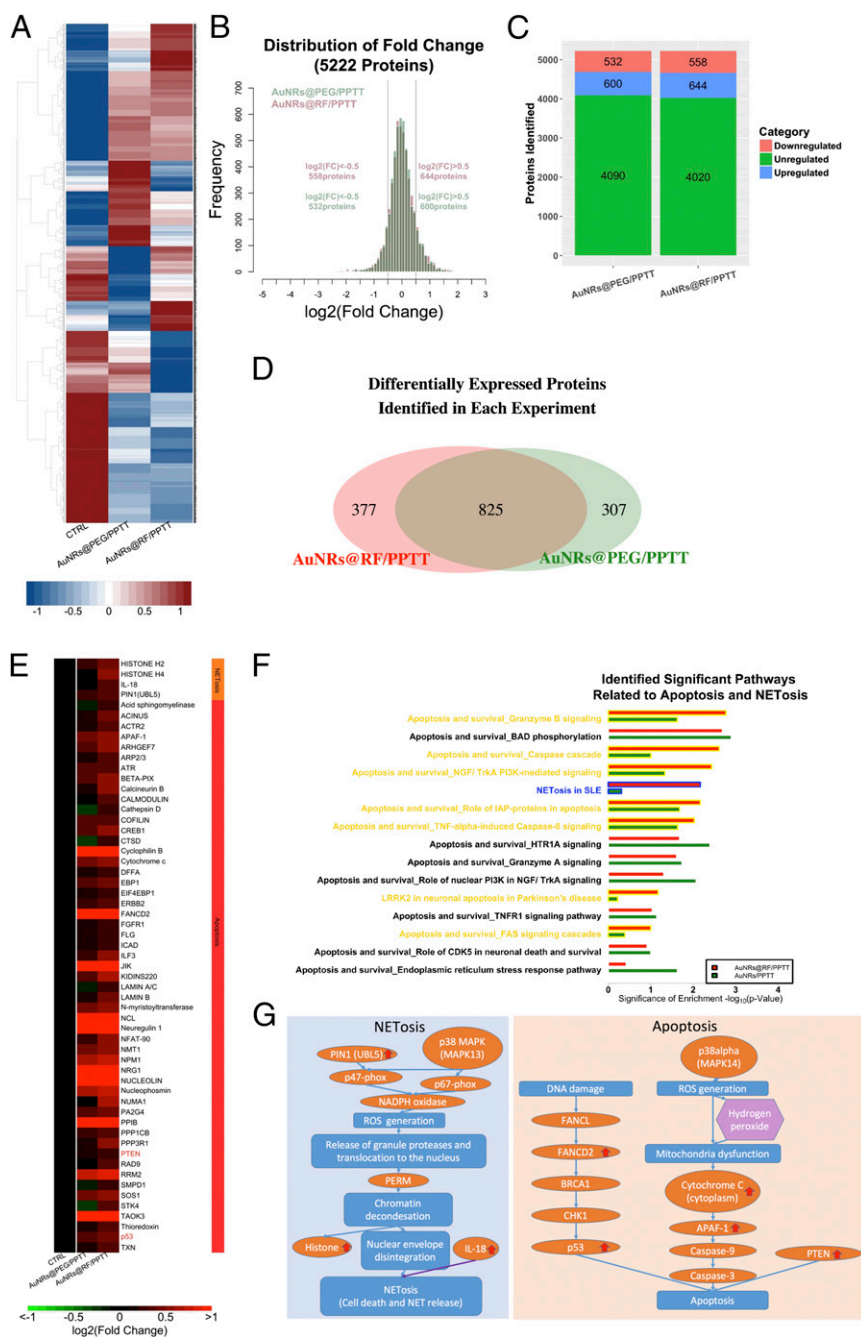
Fig. 2. Quantitative proteomics. (*A*) Comprehensive heat map showing the proteome perturbed by AuNRs@PEG-PPTT and AuNRs@RF-PPTT compared with control group. (*B*) Distribution of fold changes in proteins perturbed by AuNRs@PEG-PPTT and AuNRs@RF-PPTT compared with control group. (*C*) Bar graph showing numbers of proteins unregulated, increased, and decreased in each group. (*D*) Venn diagram showing the differentially expressed proteins identified in each group. (*E*) Heat map for proteins related to apoptosis and NETosis contributing to the better efficacy of AuNRs@RF-PPTT compared with AuNRs@PEG-PPTT. The values of protein fold change are listed in Dataset S1. (*F*) Identified significant pathways related to apoptosis and NETosis. (*G*) Simplified pathway map of NETosis and apoptosis.

treatment (Fig. 2E). These observations at the molecular level are in agreement with the phenotypic study showing that AuNRs@RF-PPTT is more effective than AuNRs@PEG-PPTT in vivo and in vitro.

Interestingly, our proteomics analysis also revealed that treatment with AuNRs@RF-PPTT induced changes in the levels of several proteins involved in the NETosis pathway more strongly than AuNRs@PEG-PPTT (Fig. 2F). NETosis refers to a specific form of neutrophil cell death caused by pathogen infection, which releases NETs (neutrophil extracellular traps). It has been recently reported that small NPs activate the NETosis pathway (53). NETosis can be triggered by two pathways: directly by IL-18 (54–56) or by chromatin decondensation (57–60).

In this study, proteomics analysis identified nine proteins in the NETosis pathway. Specifically, a clear elevation of histone H2, histone H4, IL-18, and Pin1 (peptidylprolyl cis/trans isomerase, NIMA-interacting 1) were observed following AuNRs@RF-PPTT treatment; therefore, both pathways leading to NETosis were altered (Fig. 2G). Because NETosis is related to endocytosis, we speculate that AuNRs@RF may be better taken up by cells, resulting in enhanced NETosis. In summary, from proteomics analysis we determined that AuNRs@RF-PPTT can induce apoptosis and NETosis more efficiently than AuNRs@PEG-PPTT.

Long-Term Effects of AuNRs on Biodistribution and Toxicity. Treatment with AuNRs enhanced PPTT in Balb/C mice with a low dose

Fig. 3. Effect of AuNRs on organ toxicity and accumulation. (A) Histopathological images of the liver, spleen, kidney, and lung of BALB/c mice at different time points after i.v. injection of a single dose of AuNRs (Au: 0.18 mg/kg, three mice per group). (B) TEM images at two time points AuNRs (Au: 0.18 mg/kg, three mice per group); 10,000 PEG/AuNR (indicated by arrow) were found in the liver and spleen without morphology changes (up to 15 months) when treated with 25-nm-length AuNRs. (C–F) Accumulation of AuNRs in different organs over 15 months. Au concentrations are shown in the liver (C), spleen (D), kidney (E), and lung (F) of BALB/c mice at different time points after i.v. injection of a single dose of AuNRs (Au: 0.18 mg/kg, three mice per group) (error bars are mean ± SEM).

of NIR light (Fig. 1E), indicating their strong clinical potential. However, there is limited knowledge regarding several features of this new generation of AuNRs, including their biodistribution, long-term fate, and toxicity. To assess toxicity, the histopathology of tissues from the liver, spleen, lung, and kidney of mice was evaluated by a pathologist 1 month and 15 months after single i.v. injection of AuNRs@PEG. We did not observe any histopathological abnormalities in any of the mouse organs (Fig. 3A). Furthermore, we monitored mice every week for 15 months following AuNRs@PEG injection and did not observe any clinical signs of toxicity, including ruffled fur, impeded movement, signs of abnormal constitution, aberrant behavior, loss of weight, ocular or nasal discharge, respiratory distress, inability to walk, or diarrhea. TEM was used to visually observe AuNRs@PEG particle uptake and organ tissue microstructure. As seen in Fig. 3B, AuNRs@PEG remained inside the cells without any structural changes. Measurement of Au levels in the tissues demonstrated that AuNRs@PEG were present mostly in the spleen and liver of mice (Fig. 3 C and D), and to a lesser extent in the kidney and lung (Fig. 3 E and F). To measure any gold excretion, we tested the amount of Au in the feces of mice at three different time points (1, 14, and 30 days) (Fig. S8). We found that a very small portion of injected Au was excreted, whereas the major portion of Au accumulated mainly in the spleen and liver and was sustained without any structural modification over a long period (observed up to 15 months). Au accumulated in mouse organs from the first day of treatment and remained in these tissues even 15 months later, without any evidence of toxicities.

Discussion

AuNRs-PPTT is widely recognized as a promising strategy for combating cancer. Developing a valid PPTT in vivo that triggers cancer cell apoptosis (avoiding necrosis) and exploring its molecular mechanism of action is of great importance. In addition, exploring the long-term fate of the AuNRs after treatment is critical for clinical use. In this systematic in vivo study, we (i) optimized the conditions of AuNRs-PPTT to induce apoptosis, (ii) explored the molecular mechanisms of action of AuNRs-PPTT, and (iii) revealed the long-term (15 months) fate of AuNRs, which indicated their lack of toxicity in mouse models. To optimize PPTT conditions to maximize tumor apoptosis, we evaluated the size, surface modification, and concentration of AuNRs and the PPTT laser power both in vitro (five HNSCC cell lines) and in vivo (MDA686TU xenograft mice model). Cell and tumor growth inhibition and apoptosis were clearly observed in vitro and in vivo. It is worth noting that among the five HNSCC cell lines we have used UM-SCC-47, which is a human papillomavirus-positive cell line. Our findings suggest that AuNRs-PPTT is equally effective against viral- and nonviral-derived tumors. Histopathological analysis of mice tissue revealed that a lower concentration (2.5 nM) of AuNRs@RF-PPTT significantly reduced cancer cell viability as shown by decreased Ki-67. Past attempts to induce apoptosis in vitro have applied a moderate hyperthermia (61) or targeted different cellular locations (7, 62, 63). Herein, by adjusting the surface modification and heat generation, we were able to generate efficient tumor apoptosis in vivo without any skin wounding.

In our study we have optimized our treatment dose based on the tumor volume using very low doses (in nanomolar with 100 µL AuNPs injection volume) and intratumoral injection, which is more realistic for the clinical application of PPTT. In contrast, most earlier studies injected the nanoparticles intravenously, at doses based on animal body weight (nanoparticle amount in milligrams per kilogram body weight) (8, 64, 65) Compared with other studies, we used a moderate laser intensity and low exposure time (0.5–2 W/cm^2 for 2 min) (66).

The effect of heat shock (hyperthermia) on the induction of cell apoptosis has been known for centuries. The mechanism of hyperthermia-induced apoptosis has been largely unclear until recently (67). PPTT is not simply heat shock; instead, it could be regarded as a synergistic effect between nanoparticles and hyperthermia. We observed that both apoptosis and NETosis pathways

were significantly affected after treatment with PPTT, especially AuNRs@RF-PPTT, which demonstrated a much stronger molecular impact on these pathways. Cytochrome c and p53-related apoptosis mechanisms were identified as contributing to the enhanced effect of PPTT with RF-conjugated AuNRs. Furthermore, Pin1 and IL18-related signaling contribute to the observed perturbation of the NETosis pathway by PPTT with RF-conjugated AuNRs. Up-regulation of Pin1 has been shown to induce ROS production through phosphorylation of NADPH oxidase regulatory subunits p47-phox and p67-phox (57–59). ROS production further leads to the release of PERM. Histone H4 and histone H2 are subsequently degraded, leading to chromatin decondensation, which is further enhanced by PERM. Eventually the integrity of the nuclear envelope is disrupted, resulting in cell rupturing (60). The greater effect of AuNRs@RF-PPTT on NETosis may result from better uptake of AuNRs into the cells when conjugated with RF. It has been reported recently that cells entrap nanoparticles via formation of NETs, which are formed immediately following rapid damage to plasma membranes and instability of the lysosomal compartment induced by nanoparticle stimulation (53). The significant effects observed in our study of AuNRs@RF-PPTT on the NETosis pathway may account for the greater efficacy of the RF conjugate.

After PPTT, we observed the aggregation of AuNRs@RF around cell nuclear membranes as shown by DIC microscopy (Fig. 1B). Our proteomics study identified greater up-regulation of nuclear lamin proteins (Fig. 2E), which are responsible for nuclear shape and structure. Therefore, AuNRs@RF may harm nuclear membrane integrity through intrinsic cell defense mechanisms. However, lamins are known to impede cancer cell migration and invasion (68, 69) Lamin promotes cell-matrix adhesion and plays an important role in apoptosis by loosening epithelial cell contact with the extracellular matrix (70). Lamins are targets for degradation in the apoptotic process and accordingly are often used as markers for apoptosis (71).

There is to date limited knowledge regarding the biodistribution, long-term fate, and toxicity of AuNRs. Thus, our studies of the toxicity of AuNRs are important to develop safer treatments. This is a long-term toxicity study of AuNRs in mice lasting for 15 months. Based on our findings, we can conclude that these AuNRs have great potential to be used in PPTT for the local treatment of cancers, supporting the efficient translation of AuNRs into clinical settings.

In summary, we have optimized the efficacy and studied the molecular mechanisms of AuNRs-assisted PPTT and examined the 15-month toxicity and fate of AuNRs in a mouse model. Together, these data demonstrate that our AuNRs-PPTT is highly effective and safe for local therapy for cancers. These findings provide a strong framework for translation of this approach to the clinic.

Methods

AuNRs Synthesis, Conjugation, and Characterization. A seedless growth method was used for the synthesis of AuNRs with an average size of 25 ± 3 nm × 5.5 ± 0.8 nm (length × width) (35). Briefly, HAuCl$_4$ (5.0 mL, 1.0 mM) was added to 5.0 mL of 0.2 M CTAB at room temperature. Then, 250 µL of 4.0 mM AgNO$_3$, 8 µL of 12 M HCl, and 70 µL of ascorbic acid (78.8 mM) was successively added and the solution was gently mixed. Immediately afterward, 15 µL of 0.01 M ice-cold NaBH$_4$ was injected into the unstirred growth solution and allowed to react for 12 h. The synthesized AuNRs were then centrifuged at 21,000 × g for 50 min and redispersed in deionized (DI) water, followed by a second centrifugation at 19,000 × g for 40 min to remove the extra CTAB. A seed-mediated growth method was used for the synthesis of AuNRs with an average size of 72 ± 7 nm × 16 ± 4 nm, where 4.0 mM of silver nitrate and 78.8 mM of ascorbic acid were added to a growth solution consisting of 0.2 M CTAB, 1.0 mM of HAuCl$_4$, and 0.01 M of NaBH$_4$. Then, CTAB stabilized AuNRs were purified by centrifugation (10,000 × g for 50 min) and redispersed in DI H$_2$O, followed by a second centrifugation at 7,000 × g for 30 min. For AuNRs conjugated with PEG, we added mPEG-SH (1 mM) to the nanoparticles overnight to achieve about 20,000 ligands on each particle. For AuNRs conjugated with RF, we first added 50 mL of 0.5 mM BSA (Sigma-Aldrich) to 1 nM AuNRs solution, which was then incubated for 3 h at room temperature. Then, 300 µL of 5 mM RF was added to the AuNRs solution and incubated for 3 h. After conjugation, the particles were centrifuged to remove the extra ligands. TEM was used to examine particle size

and homogeneity. UV-Vis spectrometer and ZetaSizer 3000 (Malvern Instruments) were used to examine whether the conjugation was successful. For BSA fluorescent quenching experiments, excitation and emission measurements were carried out on a Quanta Master 300 phosphorescence/fluorescence spectrofluorometer. BSA was used at a concentration of 10^{-4} M. The number of RF molecules per AuNRs was calculated according to Ali et al. (36), based on the UV-Vis spectra. The dose of AuNRs was presented as molar concentration. For comparison with other studies, 5 nM = 1 OD (35).

Dark-Field Images. MDA686TU cells were seeded on glass coverslips in complete growth medium for 24 h to achieve 40% final confluence. Cells were incubated with 2.5 nM AuNRs with RF or PEG conjugation in supplemented DMEM cell culture medium for 24 h. Dark-field images were taken using an inverted microscope equipped with a dark-field condenser and Lumenera Infinity2 CCD camera; a 20× objective lens was used to collect scattered light from the samples to produce dark-field images.

DIC Microscopy. MDA686TU cells were seeded on glass coverslips in complete growth medium for 24 h then incubated with 2.5 nM AuNRs with RF or PEG conjugation in supplemented DMEM cell culture medium for 24 h. For DIC imaging, an inverted Nikon Eclipse Ti-E microscope equipped with Perfect Focus System (PFS, 25-nm z-axial resolution) was used for imaging and z-stacks acquisitions under DIC microscopy. The DIC mode used a DIC polarizer and analyzer pair, a high-resolution 100× I-R DIC slider, a high numerical aperture (N.A. 1.40) oil-immersion condenser lens, a Nikon CFI Apo TIRF 100× (N.A. 1.49) oil-immersion objective, and a 12 V/100 W halogen lamp as light source. Appropriate bandpass filters were placed in the light path. Z-stack movies were taken by a Hamamatsu ORCA-Flash 4.0 V2 CMOS camera (C11440-22CU, pixel size 6.5 μm × 6.5 μm) with Camera Link interface using Micro-Manager and analyzed using NIH ImageJ and reconstructed in Amira. Fixed Hey cells on 22- × 22-mm glass coverslips were rinsed with Dulbecco's PBS at pH 7.4 and fabricated into a sandwiched chamber with two pieces of double-sided tape and a cleaned glass slide. PBS solution was added into the chamber to fill the space and the chamber was sealed with clear nail polish. The sample slide was then placed under the microscope for observation. Z-stacks were acquired using the multidimensional acquisition function in Micro-Manager. DIC optical sectioning (Movies S1 and S2) through the whole cell thickness was achieved by moving the objective on the motorized nosepiece using PFS at 65 nm per step at 33-ms (30 frames per s) exposure time.

Cell Lines. Information and primary sources of HNSCC cell lines MDA686TU, Fadu, and SqCC/Y1 were described elsewhere (72). UD-SCC2 and UM-SCC-47 cell lines were obtained from R. L. Ferris, University of Pittsburgh Cancer Center, Pittsburgh. Cells were maintained in DMEM/F12 (1:1) medium supplemented with 10% heat-inactivated FBS in a 37 °C, 5% CO$_2$ humidified incubator.

Cell Viability Assay. Sulforhodamine B (SRB) assay was used for cell viability determination (73). Cells were seeded (5×10^3 cells per well) in a 96-well plate. Twenty-four hours later cells were treated with AuNRs for 24 h and exposed to laser for 2 min. Cells were fixed after another 24 h. Plates were stained with SRB and bound SRB was dissolved to assess OD at 492 nm using a microplate reader. The percentage of surviving cells was calculated based on the absorbance values relative to the nontreated samples.

Apoptosis Assay. Apoptotic cells were identified and measured as described elsewhere (74). Briefly, cells were collected and stained with Annexin V-phycoerythrene and 7-AAD (BD Pharmingen) for 15 min at room temperature. Samples were measured using a FACS caliber bench-top flow cytometer (Becton Dickinson). FlowJo software (Tree Star) was used for apoptosis analysis.

Western-Blot Analysis. Western blot was incubated with primary followed by secondary antibodies and detected using enhanced chemiluminescence system as described (74). Primary antibodies were anti–phospho-Akt, anti–total Akt, anti–phospho-Erk, anti-total Erk, anti-caspase3, anti-caspase3, and anti-PARP from Cell Signaling; anti-p21 from Santa Cruz Biotechnology; and anti–β-actin from Sigma-Aldrich. Secondary antibodies were from Santa Cruz Biotechnology. Western band quantification was performed using ImageQuant TL software (GE/Amersham Biosciences).

Nude Mice Bearing Human HNSCC Xenograft Tumor Model. Based on protocols approved by the Institutional Animal Care and Use Committee of Emory University, female nude mice (athymic nu/nu) aged 4–6 wk were purchased from Taconic. Each mouse was injected with 5×10^6 MDA686TU cells s.c. in the right flank, and tumor volume was monitored (volume = $0.5 \times$ length $\times$ width^2).

Mice were randomized into groups once the tumors reached 70 mm^3. Mice were injected intratumorally with PBS or different concentrations of AuNRs and exposed to different powers of NIR laser for 2 min (five mice per group). Tumors were monitored every other day and mice were killed on the 25th day after cancer cell transplantation. Tumors and organs were collected, measured, and processed for paraffin embedding.

IHC. Upon deparaffinization and rehydration, tissue sections were permeabilized with 0.25% Triton-X-100/PBS for 5 min. Tissue sections were blocked with 2.5% horse serum for 30 min. To detect intracellular localization and expression levels of Ki-67 proteins, we used mouse anti-human Ki-67 antibody (prediluted; Invitrogen) then counterstained cell nuclei using DAPI (Invitrogen). Mouse and rabbit IgG were used as negative controls.

Sample Preparation for Proteomics. MDA686TU cells (5×10^6) were injected into the right flank of nude mice. We injected a single dose of AuNRs@PEG (2.5 nM) or AuNRs@RF (2.5 nM) intratumorally followed by 2 min of 2 W/cm^2 NIR laser exposure when the tumors had reached 150 mm^3. Twenty-four hours later we collected tumors for proteomics analysis. Each experiment was repeated twice. Mouse tumor tissues were homogenized, followed by ultrasonic tissue ablation with ice-cold lysis buffer (50 mM Hepes, pH 7.8, 150 mM NaCl 0.1% SDS, 0.5% sodium deoxycholate 1% Triton X-100 or Nonidet P-40, and phosphatase inhibitors). The cells were then scraped down and the obtained mixtures homogenized with sonication and vortexing. Cell debris was removed by centrifugation at $18,000 \times g$ for 20 min at 4 °C. Four volumes of ice-cold acetone/ethanol/acetic acid (vol/vol/vol = 50/50/0.1) was added to the supernatant to precipitate the proteins at −20 °C overnight. After centrifugation, the protein pellet was redissolved in denaturing buffer (pH 8.0) containing 8 M urea and 50 mM Hepes, and the protein concentration was tested using a Bradford assay. The disulfide bonds in the protein solution were reduced by 2 mM DTT at 37 °C for 2 h and subsequently alkylated by adding 6 mM iodoacetamide and incubation in darkness at room temperature for 40 min (75). Purified peptides were labeled with 6-plex TMT reagents (Thermo) following the manufacturer's protocol. Briefly, lyophilized peptides were dissolved in 100 μL of 100 mM triethylammonium bicarbonate buffer, pH 8.5. Each channel of the TMT reagents was dissolved in 41 μL of anhydrous ACN and transferred into the peptide tube. The reaction was performed at room temperature for 1 h then was quenched by adding 8 μL of 5% hydroxylamine. Peptides from all six tubes were then mixed, desalted again using a tC18 Sep-Pak cartridge, and lyophilized overnight. For protein analysis, the peptide mixture was separated by high pH reversed-phase HPLC into 20 fractions with a 40-min gradient of 5–55% acetonitrile (ACN) in 10 mM ammonium acetate (pH 10).

Liquid Chromatography–Tandem MS Analysis and Database Search. After TMT labeling and purification, lyophilized peptide samples were dissolved in 10 μL solvent of 5% (vol/vol) ACN and 4% (vol/vol) formic acid (FA), and 4 μL of the dissolved sample were loaded onto a microcapillary column packed with C18 beads (Magic C18AQ, 3 μm 200 Å, 100 μL × 16 cm; Michrom Bioresources) by a Dionex WPS-3000TPLRS autosampler (UltiMate 3000 thermostated Rapid Separation Pulled Loop Wellplate Sampler). Peptides were separated by reversed-phase chromatography using an UltiMate 3000 binary pump with a 90-min gradient of 4–30% (vol/vol) ACN (in 0.125% FA). Peptides were detected with a data-dependent Top15 method (76) in a hybrid dual-cell quadrupole linear ion trap–Orbitrap mass spectrometer (LTQ Orbitrap Elite; ThermoFisher, with Xcalibur 3.0.63 software). For each cycle, one full MS scan (resolution 60,000) in the Orbitrap at 106 AGC target was followed by up to 15 MS/MS for the most intense ions. The selected ions were excluded from further analysis for 90 s. Ions with single or unassigned charge were discarded. MS2 scans were performed in the orbitrap cell by activating with high energy collision dissociation at 40% normalized collision energy with 1.2 m/z isolation width. All MS2 spectra were converted into mzXML format and then searched using the SEQUEST algorithm (version 28) (77). Spectra were matched against a database containing sequences of all proteins in the UniProt Human (Homo sapiens) database. The following parameters were used during the search: 20 ppm mass tolerance; fully digested with trypsin; up to three missed cleavages; fixed modifications: carbamidomethylation of cysteine (+57.0214), TMT modification of lysine (+229.1629) and N terminus (+229.1629); variable modifications: oxidation of methionine (+15.9949). False discovery rates (FDRs) of peptide and protein identifications were evaluated and controlled by the target-decoy method (78). Each protein sequence was listed in both forward and reversed orders. Linear discriminant analysis, which is similar to other methods in the literature (79), was used to control the quality of peptide (80). Peptides fewer than seven amino acid residues in length were discarded. Furthermore, peptide

spectral matches were filtered to <1% FDR. An additional protein-level filter was applied in each dataset to reduce the protein-level FDRs (<1%).

Proteomics Data Analysis. For proteomics analysis each experiment was repeated twice. The mean expression level of each protein was used for downstream analysis. Raw data were normalized using supervised normalization of microarray (81). Variance due to biological replicates was adjusted by setting them as variables in the model. Variance explained by different experimental treatments (control, AuNRs@PEG-PPTT, and AuNRs@RF-PPTT) was fitted as a biological variable in the model. Hierarchical clustering was performed with statistical software R. Proteins identified as being affected were subjected to pathway analysis using the MetaCore from Thomson Reuters.

Short-Term and Long-Term Uptake Fate of PEGylated AuNRs. BALB/C mice (male), 6 wk of age, were injected via the tail vein with a 200-μL solution of Au NRs (0.18 mg/kg). At specified time points of 1 day, 3, 7, 14, and 30 days and 15 months mice were killed by pressurized CO_2 asphyxiation, three mice in each

group. Liver, spleen, kidney, and lung were collected, rinsed with distilled water, and dried. The dried tissues were dissolved and assayed for Au using ICP-MS.

Histopathology Evaluation. Liver, spleen, kidney, and lung tissues were embedded in paraffin and cut at 5-μm thickness. The tissues were stained with hematoxylin and eosin (Sigma) to assess histological alterations via microscopy.

Statistical Analysis. All results represent the average of at least three separate experiments and are expressed as mean ± SD or SE. Statistical analysis was conducted using t test. P values less than 0.05 were considered statistically significant.

1. Huang X, El-Sayed IH, Qian W, El-Sayed MA (2006) Cancer cell imaging and photothermal therapy in the near-infrared region by using gold nanorods. *J Am Chem Soc* 128(6):2115–2120.
2. Dickerson EB, et al. (2008) Gold nanorod assisted near-infrared plasmonic photothermal therapy (PPTT) of squamous cell carcinoma in mice. *Cancer Lett* 269(1):57–66.
3. Hirsch LR, et al. (2003) Nanoshell-mediated near-infrared thermal therapy of tumors under magnetic resonance guidance. *Proc Natl Acad Sci USA* 100(23):13549–13554.
4. Abadeer NS, Murphy CJ (2016) Recent progress in cancer thermal therapy using gold nanoparticles. *J Phys Chem C* 120(9):4691–4716.
5. Steinmetz NF (2010) Review of "Cancer Nanotechnology: Methods and Protocols (Methods in Molecular Biology)" by Stephen R. Grobmyer (Editor), Brij M. Moudgil (Editor). *BioMedical Engineering OnLine* 9:55.
6. Alkilany AM, Thompson LB, Boulos SP, Sisco PN, Murphy CJ (2012) Gold nanorods: Their potential for photothermal therapeutics and drug delivery, tempered by the complexity of their biological interactions. *Adv Drug Deliv Rev* 64(2):190–199.
7. Ali MR, Ibrahim IM, Ali HR, Selim SA, El-Sayed MA (2016) Treatment of natural mammary gland tumors in canines and felines using gold nanorods-assisted plasmonic photothermal therapy to induce tumor apoptosis. *Int J Nanomedicine* 11:4849–4863.
8. von Maltzahn G, et al. (2009) Computationally guided photothermal tumor therapy using long-circulating gold nanorod antennas. *Cancer Res* 69(9):3892–3900.
9. Pattani VP, Shah J, Atalis A, Sharma A, Tunnell JW (2015) Role of apoptosis and necrosis in cell death induced by nanoparticle-mediated photothermal therapy. *J Nanopart Res* 17(1):1–11.
10. Bonfil RD, Bustuoabad OD, Ruggiero RA, Meiss RP, Pasqualini CD (1988) Tumor necrosis can facilitate the appearance of metastases. *Clin Exp Metastasis* 6(2):121–129.
11. Hanahan D, Weinberg RA (2011) Hallmarks of cancer: The next generation. *Cell* 144(5):646–674.
12. Danial NN, Korsmeyer SJ (2004) Cell death: Critical control points. *Cell* 116(2):205–219.
13. Ali MR, Ali HR, Rankin CR, El-Sayed MA (2016) Targeting heat shock protein 70 using gold nanorods enhances cancer cell apoptosis in low dose plasmonic photothermal therapy. *Biomaterials* 102:1–8.
14. Pérez-Hernández M, et al. (2015) Dissecting the molecular mechanism of apoptosis during photothermal therapy using gold nanoprisms. *ACS Nano* 9(1):52–61.
15. Oh N, Park JH (2014) Endocytosis and exocytosis of nanoparticles in mammalian cells. *Int J Nanomedicine* 9(Suppl 1):51–63.
16. Iyer AK, Khaled G, Fang J, Maeda H (2006) Exploiting the enhanced permeability and retention effect for tumor targeting. *Drug Discov Today* 11(17-18):812–818.
17. Maeda H, Wu J, Sawa T, Matsumura Y, Hori K (2000) Tumor vascular permeability and the EPR effect in macromolecular therapeutics: a review. *J Controlled Release* 65(1-2):271–284.
18. Liu X, et al. (2013) Enhanced retention and cellular uptake of nanoparticles in tumors by controlling their aggregation behavior. *ACS Nano* 7(7):6244–6257.
19. Wilhelm S, et al. (2016) Analysis of nanoparticle delivery to tumours. *Nature Reviews Materials* 1:16014.
20. Ali MRK, Panikkanvalappil SR, El-Sayed MA (2014) Enhancing the efficiency of gold nanoparticles treatment of cancer by increasing their rate of endocytosis and cell accumulation using rifampicin. *J Am Chem Soc* 136(12):4464–4467.
21. Mackey MA, Ali MRK, Austin LA, Near RD, El-Sayed MA (2014) The most effective gold nanorod size for plasmonic photothermal therapy: Theory and in vitro experiments. *J Phys Chem B* 118(5):1319–1326.
22. Alkilany AM, Murphy CJ (2010) Toxicity and cellular uptake of gold nanoparticles: What we have learned so far? *J Nanopart Res* 12(7):2313–2333.
23. Connor EE, Mwamuka J, Gole A, Murphy CJ, Wyatt MD (2005) Gold nanoparticles are taken up by human cells but do not cause acute cytotoxicity. *Small* 1(3):325–327.
24. Axiak-Bechtel SM, et al. (2014) Gum arabic-coated radioactive gold nanoparticles cause no short-term local or systemic toxicity in the clinically relevant canine model of prostate cancer. *Int J Nanomedicine* 9:5001–5011.
25. Chen H, et al. (2013) In vivo study of spherical gold nanoparticles: Inflammatory effects and distribution in mice. *PLoS One* 8(2):e58208.
26. You J, et al. (2014) Pharmacokinetics, clearance, and biosafety of polyethylene glycol-coated hollow gold nanospheres. *Part Fibre Toxicol* 11:26.
27. Pernodet N, et al. (2006) Adverse effects of citrate/gold nanoparticles on human dermal fibroblasts. *Small* 2(6):766–773.
28. Cho YS, et al. (2009) Phosphorylation-driven assembly of the RIP1-RIP3 complex regulates programmed necrosis and virus-induced inflammation. *Cell* 137(6):1112–1123.
29. Qu Y, Huang Y, Lü X (2013) Proteomic analysis of molecular biocompatibility of gold nanoparticles to human dermal fibroblasts-fetal. *J Biomed Nanotechnol* 9(1):40–52.
30. Yildirimer L, Thanh NTK, Loizidou M, Seifalian AM (2011) Toxicology and clinical potential of nanoparticles. *Nano Today* 6(6):585–607.
31. Murphy CJ, et al. (2008) Gold nanoparticles in biology: Beyond toxicity to cellular imaging. *Acc Chem Res* 41(12):1721–1730.
32. Boisselier E, Astruc D (2009) Gold nanoparticles in nanomedicine: Preparations, imaging, diagnostics, therapies and toxicity. *Chem Soc Rev* 38(6):1759–1782.
33. Niidome T, et al. (2006) PEG-modified gold nanorods with a stealth character for in vivo applications. *J Control Release* 114(3):343–347.
34. Sadauskas E, et al. (2009) Protracted elimination of gold nanoparticles from mouse liver. *Nanomedicine (Lond)* 5(2):162–169.
35. Ali MRK, Snyder B, El-Sayed MA (2012) Synthesis and optical properties of small Au nanorods using a seedless growth technique. *Langmuir* 28(25):9807–9815.
36. Ali HR, et al. (2016) Gold nanorods as drug delivery vehicles for rifampicin greatly improve the efficacy of combating Mycobacterium tuberculosis with good biocompatibility with the host cells. *Bioconjug Chem* 27(10):2486–2492.
37. Sakai T, et al. (2004) Nucling recruits Apaf-1/pro-caspase-9 complex for the induction of stress-induced apoptosis. *J Biol Chem* 279(39):41131–41140.
38. Yin Q, et al. (2006) Caspase-9 holoenzyme is a specific and optimal procaspase-3 processing machine. *Mol Cell* 22(2):259–268.
39. Geering B, Simon HU (2011) A novel signaling pathway in TNFα-induced neutrophil apoptosis. *Cell Cycle* 10(17):2821–2822.
40. Geering B, Gurzeler U, Federzoni E, Kaufmann T, Simon HU (2011) A novel TNFR1-triggered apoptosis pathway mediated by class IA PI3Ks in neutrophils. *Blood* 117(22):5953–5962.
41. Barroso E, et al. (2009) The Fanconi anemia family of genes and its correlation with breast cancer susceptibility and breast cancer features. *Breast Cancer Res Treat* 118(3):655–660.
42. Montes de Oca R, et al. (2005) Regulated interaction of the Fanconi anemia protein, FANCD2, with chromatin. *Blood* 105(3):1003–1009.
43. Longerich S, San Filippo J, Liu D, Sung P (2009) FANCI binds branched DNA and is monoubiquitinated by UBE2T-FANCL. *J Biol Chem* 284(35):23182–23186.
44. Yuan F, El Hokayem J, Zhou W, Zhang Y (2009) FANCI protein binds to DNA and interacts with FANCD2 to recognize branched structures. *J Biol Chem* 284(36):24443–24452.
45. Garcia-Higuera I, et al. (2001) Interaction of the Fanconi anemia proteins and BRCA1 in a common pathway. *Mol Cell* 7(2):249–262.
46. Taniguchi T, et al. (2002) S-phase-specific interaction of the Fanconi anemia protein, FANCD2, with BRCA1 and RAD51. *Blood* 100(7):2414–2420.
47. Yarden RI, Pardo-Reoyo S, Sgagias M, Cowan KH, Brody LC (2002) BRCA1 regulates the G2/M checkpoint by activating Chk1 kinase upon DNA damage. *Nat Genet* 30(3):285–289.
48. Goudelock DM, Jiang K, Pereira E, Russell B, Sanchez Y (2003) Regulatory interactions between the checkpoint kinase Chk1 and the proteins of the DNA-dependent protein kinase complex. *J Biol Chem* 278(32):29940–29947.
49. Norbury CJ, Zhivotovsky B (2004) DNA damage-induced apoptosis. *Oncogene* 23(16):2797–2808.
50. Weng L, Brown J, Eng C (2001) PTEN induces apoptosis and cell cycle arrest through phosphoinositol-3-kinase/Akt-dependent and -independent pathways. *Hum Mol Genet* 10(3):237–242.
51. Qi Y, et al. (2015) PTEN induces apoptosis and cavitation via HIF-2-dependent Bnip3 upregulation during epithelial lumen formation. *Cell Death Differ* 22(5):875–884.
52. Zhao H, Dupont J, Yakar S, Karas M, LeRoith D (2004) PTEN inhibits cell proliferation and induces apoptosis by downregulating cell surface IGF-IR expression in prostate cancer cells. *Oncogene* 23(3):786–794.

53. Muñoz LE, et al. (2016) Nanoparticles size-dependently initiate self-limiting NETosis-driven inflammation. *Proc Natl Acad Sci USA* 113(40):E5856–E5865.

54. Yu Y, Su K (2013) Neutrophil extracellular traps and systemic lupus erythematosus. *J Clin Cell Immunol* 4:4.

55. Kahlenberg JM, Carmona-Rivera C, Smith CK, Kaplan MJ (2013) Neutrophil extracellular trap-associated protein activation of the NLRP3 inflammasome is enhanced in lupus macrophages. *J Immunol* 190(3):1217–1226.

56. Mitroulis I, et al. (2011) Neutrophil extracellular trap formation is associated with IL-1β and autophagy-related signaling in gout. *PLoS One* 6(12):e29318.

57. Makni-Maalej K, et al. (2012) The TLR7/8 agonist CL097 primes N-formyl-methionyl-leucyl-phenylalanine-stimulated NADPH oxidase activation in human neutrophils: Critical role of p47phox phosphorylation and the proline isomerase Pin1. *J Immunol* 189(9):4657–4665.

58. El Benna J, et al. (1996) Activation of p38 in stimulated human neutrophils: Phosphorylation of the oxidase component p47phox by p38 and ERK but not by JNK. *Arch Biochem Biophys* 334(2):395–400.

59. Dang PM, Morel F, Gougerot-Pocidalo MA, El Benna J (2003) Phosphorylation of the NADPH oxidase component p67(PHOX) by ERK2 and P38MAPK: Selectivity of phosphorylated sites and existence of an intramolecular regulatory domain in the tetratricopeptide-rich region. *Biochemistry* 42(15):4520–4526.

60. Papayannopoulos V, Metzler KD, Hakkim A, Zychlinsky A (2010) Neutrophil elastase and myeloperoxidase regulate the formation of neutrophil extracellular traps. *J Cell Biol* 191(3):677–691.

61. Li S, Chien S, Branemark PI (1999) Heat shock-induced necrosis and apoptosis in osteoblasts. *J Orthopaedic Res* 17(6):891–899.

62. Wang L, et al. (2011) Selective targeting of gold nanorods at the mitochondria of cancer cells: Implications for cancer therapy. *Nano Lett* 11(2):772–780.

63. Kang B, Mackey MA, El-Sayed MA (2010) Nuclear targeting of gold nanoparticles in cancer cells induces DNA damage, causing cytokinesis arrest and apoptosis. *J Am Chem Soc* 132(5):1517–1519.

64. Lal S, Clare SE, Halas NJ (2008) Nanoshell-enabled photothermal cancer therapy: Impending clinical impact. *Acc Chem Res* 41(12):1842–1851.

65. Melancon MP, et al. (2008) In vitro and in vivo targeting of hollow gold nanoshells directed at epidermal growth factor receptor for photothermal ablation therapy. *Mol Cancer Ther* 7(6):1730–1739.

66. Moon HK, Lee SH, Choi HC (2009) In vivo near-infrared mediated tumor destruction by photothermal effect of carbon nanotubes. *ACS Nano* 3(11):3707–3713.

67. Song AS, Najjar AM, Diller KR (2014) Thermally induced apoptosis, necrosis, and heat shock protein expression in 3D culture. *J Biomech Eng* 136(7):071006-1–071006-10.

68. Short B (2014) Lamin-A provides stiff resistance to cell migration. *J Cell Biol* 204(5):626.

69. van der Zee JA, et al. (2012) Tumour basement membrane laminin expression predicts outcome following curative resection of pancreatic head cancer. *Br J Cancer* 107(7):1153–1158.

70. Esco MA, Wang Z, McDermott ML, Kurpakus-Wheater M (2001) Potential role for laminin 5 in hypoxia-mediated apoptosis of human corneal epithelial cells. *J Cell Sci* 114(Pt 22):4033–4040.

71. Broers JL, Ramaekers FC (2014) The role of the nuclear lamina in cancer and apoptosis. *Adv Exp Med Biol* 773:27–48.

72. Zhao M, et al. (2011) Assembly and initial characterization of a panel of 85 genomically validated cell lines from diverse head and neck tumor sites. *Clin Cancer Res* 17(23):7248–7264.

73. Vichai V, Kirtikara K (2006) Sulforhodamine B colorimetric assay for cytotoxicity screening. *Nat Protoc* 1(3):1112–1116.

74. Rahman MA, et al. (2013) RRM2 regulates Bcl-2 in head and neck and lung cancers: A potential target for cancer therapy. *Clin Cancer Res* 19(13):3416–3428.

75. Wu Y, et al. (2014) Five-plex isotope dimethyl labeling for quantitative proteomics. *Chem Commun (Camb)* 50(14):1708–1710.

76. Xiao H, Wu R (2016) Quantitative investigation of human cell surface N-glycoprotein dynamics. *Chem Sci (Camb)* 8:268–277.

77. Eng JK, McCormack AL, Yates JR (1994) An approach to correlate tandem mass spectral data of peptides with amino acid sequences in a protein database. *J Am Soc Mass Spectrom* 5(11):976–989.

78. Elias JE, Gygi SP (2007) Target-decoy search strategy for increased confidence in large-scale protein identifications by mass spectrometry. *Nat Methods* 4(3):207–214.

79. Käll L, Canterbury JD, Weston J, Noble WS, MacCoss MJ (2007) Semi-supervised learning for peptide identification from shotgun proteomics datasets. *Nat Methods* 4(11):923–925.

80. Huttlin EL, et al. (2010) A tissue-specific atlas of mouse protein phosphorylation and expression. *Cell* 143(7):1174–1189.

81. Mecham BH, Nelson PS, Storey JD (2010) Supervised normalization of microarrays. *Bioinformatics* 26(10):1308–1315.